Geochemistry, Geophysics, Geosystems®

RESEARCH ARTICLE
10.1029/2022GC010385

High Heat Flow Anomaly Within the St Paul Fracture Zone: Heat Advection and/or Inherent Thermal Structure?

Emma P. M. Gregory[1,2], Heinrich Villinger[3], Satish C. Singh[1], and Norbert Kaul[3]

[1]Institut de Physique du Globe de Paris, CNRS, Université de Paris Cité, Paris, France, [2]Now at Ocean Environment Team, UK Hydrographic Office, Taunton, UK, [3]Department of Geosciences, University of Bremen, Bremen, Germany

Key Points:

- A high heat flow anomaly of 10–15 mWm^{-2} is observed in the St Paul fracture zone compared to the adjacent oceanic crust
- The heat flow anomaly is likely due to tectonically driven fluid flow but thermal rejuvenation at the transform fault could also contribute
- Fracture zones may act as high permeability pathways for fluid flow, and form and evolve differently to standard oceanic lithosphere

Supporting Information:

Supporting Information may be found in the online version of this article.

Correspondence to:

E. P. M. Gregory,
epmgregory@gmail.com

Citation:

Gregory, E. P. M., Villinger, H., Singh, S. C., & Kaul, N. (2023). High heat flow anomaly within the St Paul fracture zone: Heat advection and/or inherent thermal structure? *Geochemistry, Geophysics, Geosystems*, *24*, e2022GC010385. https://doi.org/10.1029/2022GC010385

Received 11 FEB 2022
Accepted 28 JUN 2022

Abstract Heat flow across oceanic transform faults (TFs) and fracture zones (FZs) has rarely been studied in detail, despite these features representing distinct thermal boundaries within the oceanic lithosphere. Here, we present heat flow measurements across the St Paul fracture zone (SPFZ) in the equatorial Atlantic Ocean, from 48 Ma crust in the south to 71 Ma in the north. To the north of the FZ we find a basal heat flow of 63 mWm^{-2}, and to the south a basal heat flow of 79 mWm^{-2}, both in agreement with plate cooling models. However, within the SPFZ we find a heat flow of 83 mWm^{-2}, greater than the values of the adjacent crust and 10–15 mWm^{-2} higher than predicted from conductive cooling models, suggesting that the thermal structure of the FZ has been modified. Evidence from seismic and sub-bottom profiler data indicate recent active deformation within the SPFZ, potentially driven by lithospheric flexure across the FZ or temporal changes in TF configuration. We propose that this deformation may enable fluid circulation and heat advection within the basement, creating the seafloor heat flow anomaly within the FZ. These findings suggest that FZs may remain important zones predisposed to host deformation and fluid flow in the oceanic lithosphere, despite not being active plate boundaries.

1. Introduction

Oceanic transform faults (TFs) and fracture zones (FZs) are prominent features of the mid-ocean ridge system and ocean basins. TFs are seismologically active strike-slip plate boundaries connecting two segments of a spreading center, and hence they are expected to exhibit increased heat flow as compared to the adjacent crust (Behn et al., 2007). On the other hand, FZs are generally seismically inactive intra-plate discontinuities, representing the extinct traces of TFs. However, FZs represent distinct and abrupt changes in lithospheric age within a rigid plate and therefore also mark changes in lithospheric thickness, density and thermal structure. These contrasts are especially significant at slow-spreading ridges where TFs often exhibit large age-offsets. The persistent relief of FZs as they age suggests the influence of lithospheric flexural adjustments (Sandwell, 1984) and differential subsidence (De Long et al., 1977), which are dependent on age-offset across the FZ, indicating that these features may experience long-lasting tectonic processes. Transform faults and FZs have also been suggested as potential host locations for the deep biosphere and early life forms (Cannat et al., 1991; Hensen et al., 2019; Stakes et al., 2002), and places for fluid and chemical exchange between the lithosphere and the ocean (Gregory et al., 2021; Hensen et al., 2022; Kohli et al., 2021), with heat and fluid flow conditions within the crust crucial to these important processes. Despite their significance, no methodical heat flow surveys have been conducted across either TFs or FZs aside from a study of the young Ecuador FZ in the equatorial Pacific Ocean, dominated by shallow outcrop-to-outcrop flow (Kolandaivelu et al., 2017). Here, we present a systematic heat flow study across the St Paul FZ.

The St Paul TF system offsets the Mid-Atlantic Ridge (MAR) in the equatorial Atlantic Ocean (Figure 1a) and exhibits a complex configuration comprising three intra-transform spreading segments separated by four TFs (Maia et al., 2016). The St Paul together with the Romanche and Chain TFs offset the MAR by over 1,700 km, with a total age-offset of 90 Myr, and have been active since the opening of the equatorial Atlantic Ocean during the Late Jurassic epoch through a trans-extensional regime. The St Paul TF system currently offsets the MAR by ~560 km, with the northern-most fault encompassing ~300 km of the total. The present half-spreading rate is ~12 mm/a but has varied over the past 80 Ma up to 25 mm/a (Müller et al., 2008). Our study area focusses on the inactive northern-most FZ ~1,000 km east of the eastern ridge-transform intersection, where the FZ juxtaposes 48 Ma lithosphere to the south against 71 Ma (Müller et al., 2016) lithosphere to the north (Figure 1b). At this location, only two FZs are present, with the second located ~60 km to the south, indicating a change in

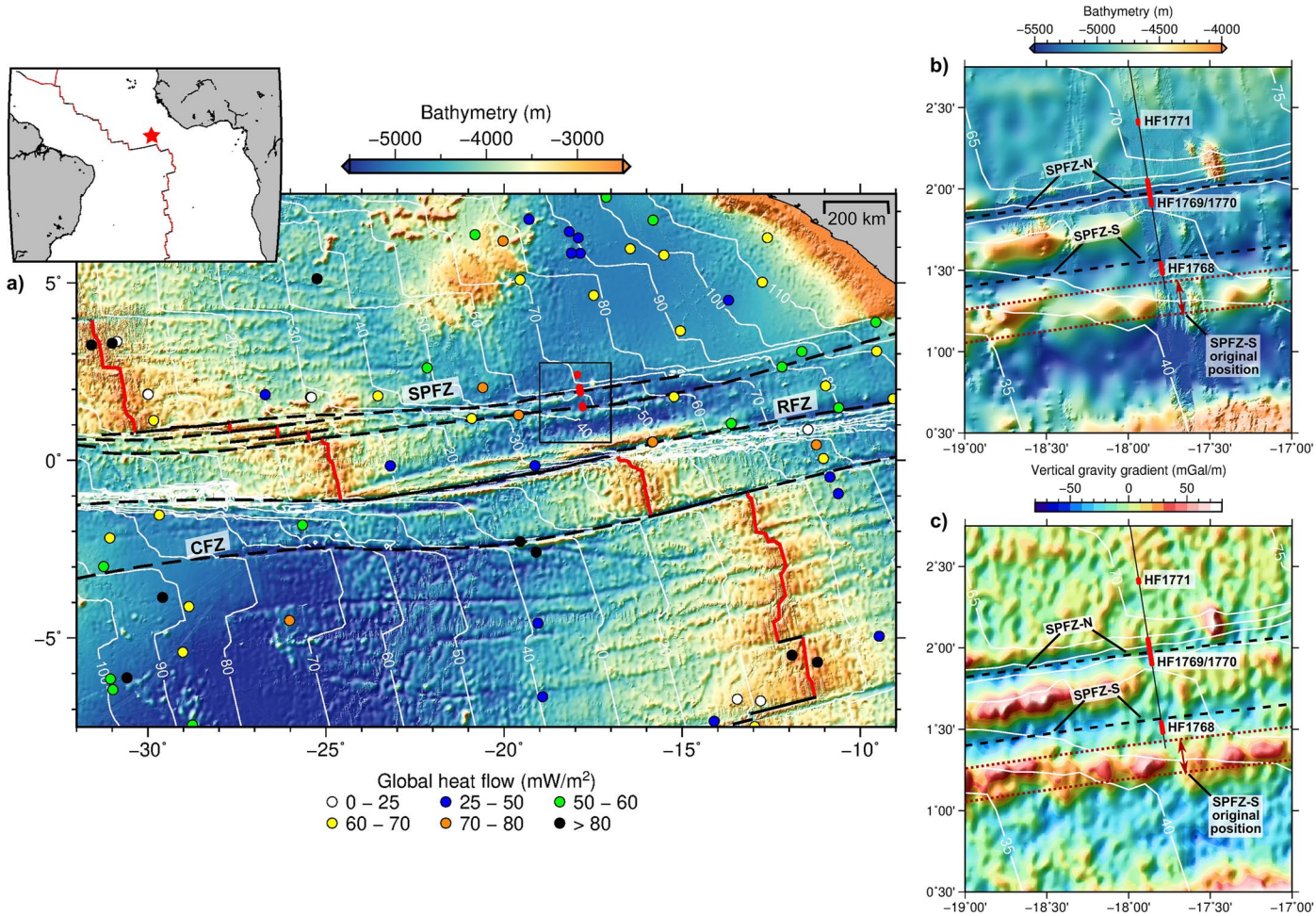

Figure 1. Study area of the heat flow survey. (a) Bathymetry of the equatorial Atlantic Ocean (GEBCO Compilation Group, 2019), showing the location of the heat flow sites from this study (red circles). Also shown are the Mid-Atlantic Ridge (red solid line); transform faults (black solid line); major equatorial fracture zones (FZs) (black dashed line); and previously published heat flow values (color-coded circles—International Heat Flow Commission, 2012). SPFZ: St Paul Fracture Zone; RFZ: Romanche Fracture Zone; and CFZ: Chain Fracture Zone. Plate age in Ma is shown by labeled white contours (Müller et al., 2019). Black box is the area shown in panels (b) and (c). Inset shows the location of the study area (red star) in the wider Atlantic region. (b) Detailed multibeam swath bathymetry of the study area, showing the seismic profile from Mehouachi and Singh (2018) (black line) and heat flow measurement locations (red circles), labeled with the site names. Also shown as black dashed lines are the locations of the northern and southern St Paul Fracture Zones (SPFZ-N and SPFZ-S, respectively), as defined in this study. Plate age in Ma from the global models is shown by white contours (Müller et al., 2019), with the original position of the SPFZ-S indicated by this age model shown by the dark red dotted lines and arrow. Note how the heat flow site HF1768 lies to the south of the new SPFZ-S position, as opposed to the north of the original position. (c) Vertical gravity gradient (Sandwell et al., 2014) of the study area, showing the locations of the two FZs as proposed in this study (black dashed lines).

ridge-transform configuration over time. The profile is co-located with a deep seismic reflection study, where the base of the lithosphere is imaged at 77 km below the seafloor south of the FZ and deepens linearly to 85 km north of the FZ (Mehouachi & Singh, 2018).

If FZs are truly tectonically inactive features and cool conductively, one would expect the heat flow to vary linearly across the FZ due to lateral conduction. However, active fluid flow, if present, would disturb this pattern (e.g., Stein & Stein, 1994). Furthermore, some recent studies have indicated that the lithospheric structure of TF systems might be more complex (Wang et al., 2022) and crustal thickening by lateral melt sill injection might occur at ridge-transform intersections (Grevemeyer et al., 2021; Growe et al., 2021; Marjanović et al., 2020). This process would lead to rejuvenation of the lithosphere, which is then likely to age and evolve differently to standard oceanic crust. In order to test whether the simple conductive model is valid or not along FZs, we acquired heat flow data across the St Paul FZ (Figure 1).

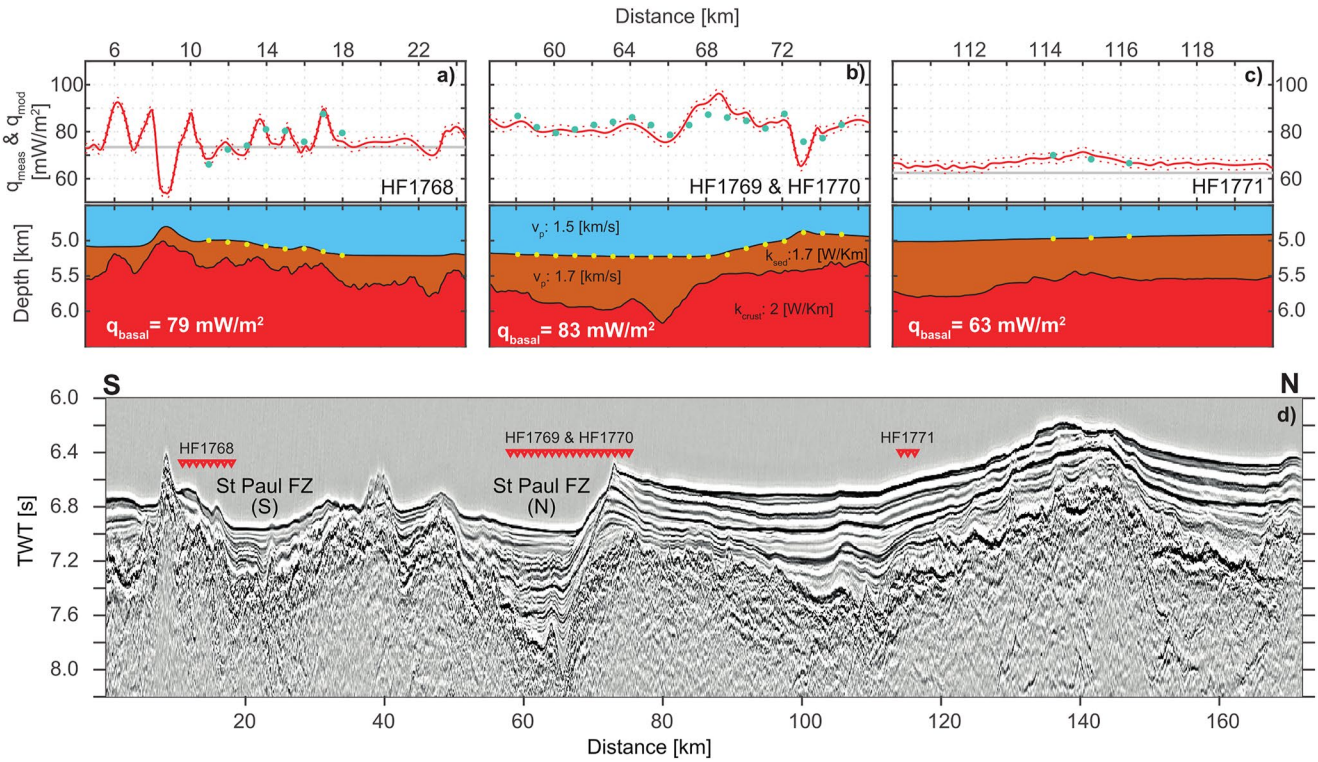

Figure 2. Heat flow and seismic image. (a–c) Measured seafloor heat flow values (blue circles) compared with modeled heat flow (red solid line). Dotted red lines represent an error of ±2 mWm^{-2} from the modeled heat flow. Heat flow predicted by the plate cooling model (Hasterok, 2013) is shown by the solid gray line. The subsurface model used to calculate the modeled heat flow is shown beneath the graphs: showing water column (blue), sediments (brown), and igneous basement (red), labeled with parameters used during the calculations and the resultant best-fit basal heat flow, with yellow circles representing the measurement locations. The modeled heat flow shows a good fit to the measured values and local variation at each site. (d) Seismic reflection image along the heat flow profile (Mehouachi & Singh, 2018), showing the along-profile locations of the measurements (red inverted triangles). The main, northern St Paul fracture zone (FZ) is labeled as St Paul FZ (N), and the suggested new location for the second, southern FZ is labeled as St Paul FZ (S).

2. Data and Methods

The heat flow data were acquired in 2017 aboard the German R/V Maria S. Merian, alongside multibeam bathymetry and sub-bottom profiler (sediment echosounder) data (Grevemeyer et al., 2019). Coincident seismic reflection data were also used here to analyze the sedimentary structures, with seismic acquisition details given in Mehouachi and Singh (2018).

2.1. Bathymetry and Sediment Echosounding Data

High-resolution multibeam bathymetry data in the study area (Figure 1b) were acquired using a Kongsberg EM122 system at a resolution of 50 m. Sub-bottom sediment echosounder (Parasound system) data provide a high-resolution single-channel image of the upper ~100 m (~0.1 s TWT) of the sedimentary cover, with a lateral resolution of 14 m (average ping spacing).

2.2. Heat Flow Survey

Twenty-nine heat flow measurements were made at three sites located on a north-south profile across the St Paul FZ (Figure 1b), with one joint site within the 20 km-wide FZ valley (HF1769 and HF1770) and the other two located ~50 km to the north (HF1771) and south (HF1768) of the FZ. From the seismic reflection images (Figure 2), we can observe that the whole profile is covered with a thick layer of sediment. Sediment thickness ranges from 320 to 990 m within the FZ valley (average ~600 m), 110–345 m at the southern site (average ~240 m) and 590–730 m at the northern site (average ~620 m). Heat flow measurements were conducted using the 6 m-long Bremen heat flow probe (Villinger et al., 2010), which is constructed in the classical violin bow

Table 1
Measured Heat Flow Values

ID	Latitude °	Latitude Minute	Longitude °	Longitude Minute	Depth (m)	N	dT/dz (mK/m)	k (W/Km)	q (mW/m^2)
HF1768									
HF1768P01	1	28.803	−17	47.395	5,043	21	71.85	0.92 ± 0.01	66.1 ± 0.7
HF1768P02	1	29.339	−17	47.490	5,069	21	80.06	0.90 ± 0.01	72.4 ± 1.0
HF1768P03	1	29.876	−17	47.575	5,100	21	83.21	0.89 ± 0.01	74.1 ± 0.8
HF1768P04	1	30.415	−17	47.653	5,123	20	92.05	0.88 ± 0.01	81.0 ± 0.9
HF1768P05	1	30.954	−17	47.739	5,164	21	91.75	0.87 ± 0.01	80.3 ± 1.0
HF1768P06	1	31.491	−17	47.825	5,160	21	88.03	0.86 ± 0.01	75.7 ± 0.9
HF1768P07	1	32.028	−17	47.912	5,201	20	104.27	0.84 ± 0.01	87.6 ± 1.0
HF1768P08	1	32.564	−17	47.996	5,256	21	96.00	0.82 ± 0.01	79.5 ± 0.8
HF1769									
HF1769P01	1	54.049	−17	51.428	5,263	21	104.48	0.83 ± 0.01	86.7 ± 1.0
HF1769P02	1	54.587	−17	51.515	5,267	21	98.82	0.83 ± 0.01	81.9 ± 1.1
HF1769P03	1	55.123	−17	51.599	5,280	20	95.75	0.83 ± 0.01	79.5 ± 1.0
HF1769P04	1	55.660	−17	51.685	5,278	20	94.36	0.84 ± 0.01	81.0 ± 1.1
HF1769P05	1	56.197	−17	51.771	5,281	21	96.38	0.86 ± 0.01	82.9 ± 1.0
HF1769P06	1	56.734	−17	51.857	5,291	21	94.55	0.89 ± 0.01	84.2 ± 0.9
HF1769P07	1	57.272	−17	51.943	5,292	21	93.12	0.92 ± 0.01	86.1 ± 1.0
HF1770									
HF1770P01	1	57.805	−17	52.029	5,299	20	91.04	0.91 ± 0.01	82.9 ± 0.9
HF1770P02	1	58.343	−17	52.115	5,288	20	87.23	0.90 ± 0.01	78.7 ± 1.0
HF1770P03	1	58.880	−17	52.200	5,294	20	92.02	0.90 ± 0.01	82.8 ± 0.9
HF1770P04	1	59.417	−17	52.285	5,292	21	97.45	0.89 ± 0.01	87.3 ± 1.1
HF1770P05	1	59.954	−17	52.371	5,268	20	94.54	0.91 ± 0.01	86.0 ± 0.9
HF1770P06	2	00.491	−17	52.457	5,179	19	90.03	0.94 ± 0.01	84.6 ± 0.9
HF1770P07	2	1.028	−17	52.544	5,122	19	85.17	0.96 ± 0.01	81.4 ± 1.2
HF1770P08	2	1.565	−17	52.629	5,077	16	91.26	0.96 ± 0.02	87.6 ± 1.8
HF1770P09	2	2.104	−17	52.715	4,952	9	79.67	0.96 ± 0.02	76.2 ± 1.9
HF1770P10	2	2.642	−17	52.800	4,963	15	77.26	1.00 ± 0.02	77.3 ± 1.5
HF1770P11	2	3.177	−17	52.888	4,980	16	78.26	1.04 ± 0.02	83.0 ± 1.4
HF1771									
HF1771P01	2	24.123	−17	56.243	5,044	10	73.69	0.95 ± 0.02	70.0 ± 1.5
HF1771P02	2	24.659	−17	56.321	5,033	11	71.29	0.95 ± 0.02	68.0 ± 1.5
HF1771P03	2	25.196	−17	56.405	5,012	11	70.13	0.95 ± 0.02	66.6 ± 1.4

Note. N: number of measurements along the probe; dT/dz: vertical temperature gradient; k: mean thermal conductivity and standard error in the mean; q: vertical component of heat flow and error. Thermal conductivities in blue are interpolated values based on adjacent measured values.

design (Hartmann & Villinger, 2002; Hyndman et al., 1979). The probe contains 21 thermistors distributed over a total length of 6 m in a sensor tube, which also contains a heater wire for in situ thermal conductivity measurements (Lister, 1979). Measurements were made in a pogo-style fashion as described in Hyndman et al. (1979) with a measurement spacing of ∼1 km. In situ thermal conductivity was measured at almost every second penetration and the mean value calculated from the thermal conductivity profile at each site. Interpolated values of the adjacent measurements were used for the intervening stations. All the seafloor heat flow measurements (Table 1,

Table 2
Parameters of the Plate Cooling Model Used in This Study After Hasterok (2013) and Mehouachi and Singh (2018)

Parameter	Value		Unit
	Hasterok (2013)	Mehouachi and Singh (2018)	
Thermal conductivity	3.5	3.138	$W\ m^{-1}\ K^{-1}$
Thermal diffusivity	9	8	$10^{-7}\ m^2\ s^{-1}$
Density	3,300	3,330	$kg\ m^{-3}$
Specific heat capacity	1170	1170	$J\ kg^{-1}\ K^{-1}$
Lithosphere thickness	90	106	km
Mantle temperature	1364	1415	°C

Figure 2; for a compilation of all temperature profiles see Figure S1) are of high quality with the probe penetrating to full length within the sediment. Basic processing of the data followed the steps outlined in Hyndman et al. (1979), Villinger and Davis (1987), and Villinger et al. (2010). As precise positioning of the probe at the seafloor using an ultra-short baseline system was not possible due to technical problems, the ship's position was instead taken as the location of the probe on the seafloor.

2.3. Thermal Modeling

Measured surface heat flow can vary locally as a function of seafloor topography, basement topography, and the thermal conductivity contrast between the sediment and basement. To understand these local effects and calculate true variations in the basal heat flow, taking variations in topography into account, we conducted numerical modeling of the conductive regime at the St Paul FZ. For each site, we created a steady-state 2D purely conductive finite element model with the geometry defined by the seismic profile, using a sediment velocity of 1,700 m/s to calculate sediment thickness (e.g., Christeson et al., 2016; Swift et al., 1998). Constant thermal conductivities of 1.7 and 2.0 $Wm^{-1}K^{-1}$ and zero heat production were assigned to the sediments and lithosphere, respectively (e.g., Pribnow et al., 2000). The heat flow into the model at the base of the lithosphere (basal heat flow) was iteratively adjusted for each site until the misfit between the observed and calculated heat flow was minimal, with the final value assumed as a representative heat flow value for each site. The estimated uncertainty in the basal heat flow is $\pm 2\ mWm^{-2}$, assuming realistic uncertainties of $\pm 100\ ms^{-1}$ in sediment velocity and ±10% in thermal conductivity.

2.4. Conductive Geotherms

Predicted temperature-depth profiles and surface heat flow were calculated using two different plate cooling models (Table 2) and the plate ages from Müller et al. (2016). The Hasterok (2013) model is constrained by global observations of surface heat flow and seafloor subsidence. The model proposed by Mehouachi and Singh (2018) is based on the plate cooling model of McKenzie et al. (2005) and was used to calculate lithosphere-asthenosphere boundary (LAB) temperatures along the St Paul FZ profile, and uses slightly different thermal and lithospheric parameters. The different models produce similar values for the predicted heat flow for both north of the FZ: 62 versus 59 mWm^{-2} for the models from Hasterok (2013) and Mehouachi and Singh (2018), respectively; and for the lithosphere south of the FZ: 73 versus 72 mWm^{-2}. Errors in the predicted heat flow result from errors in crustal age and plate thickness (depth to the LAB). Here, the LAB depth is well constrained within ±2 km (Mehouachi & Singh, 2018). However, the error in plate age from the global models could vary up to ±4–6 Myr (Müller et al., 2008), as crustal age between ~15°N and ~5°S in the equatorial Atlantic Ocean cannot be constrained by magnetic lineations due to the north-south strike of the ridge and its equatorial location (Seton et al., 2014). Instead, crustal age is based on reconstruction using finite rotations, resulting in larger errors in age than further north or south of the equator. Across our profile, the global model places the southerly St Paul Fracture Zone (SPFZ-S) at ~1°20′N, which is south of heat flow site HF1768, resulting in an average age of ~48 Ma for this site. However, satellite gravity (Sandwell et al., 2014), our multibeam bathymetry and seismic reflection profiles indicate that the FZ is most likely located at 1°34′N, corresponding to ~20 km along our profile (Figures 1 and 2d). This new location is just north of heat flow site HF1768, suggesting that the age of the lithosphere at this site is likely that of the plate to the south of the FZ system (~41 Ma), rather than that of the sliver of lithosphere between the two FZs as given by the global plate age model (~48 Ma). We calculated the predicted heat flow using both ages for this site.

3. Results

Measured surface heat flow varies between 60 and 90 mWm^{-2} (Table 1, Figures 2a–2c). All temperature-depth profiles are linear (see Figure S1), indicating steady-state conductive heat transport within the sediments. In general, the observed seafloor heat variations agree well with the modeled heat flow, with an average RMS misfit

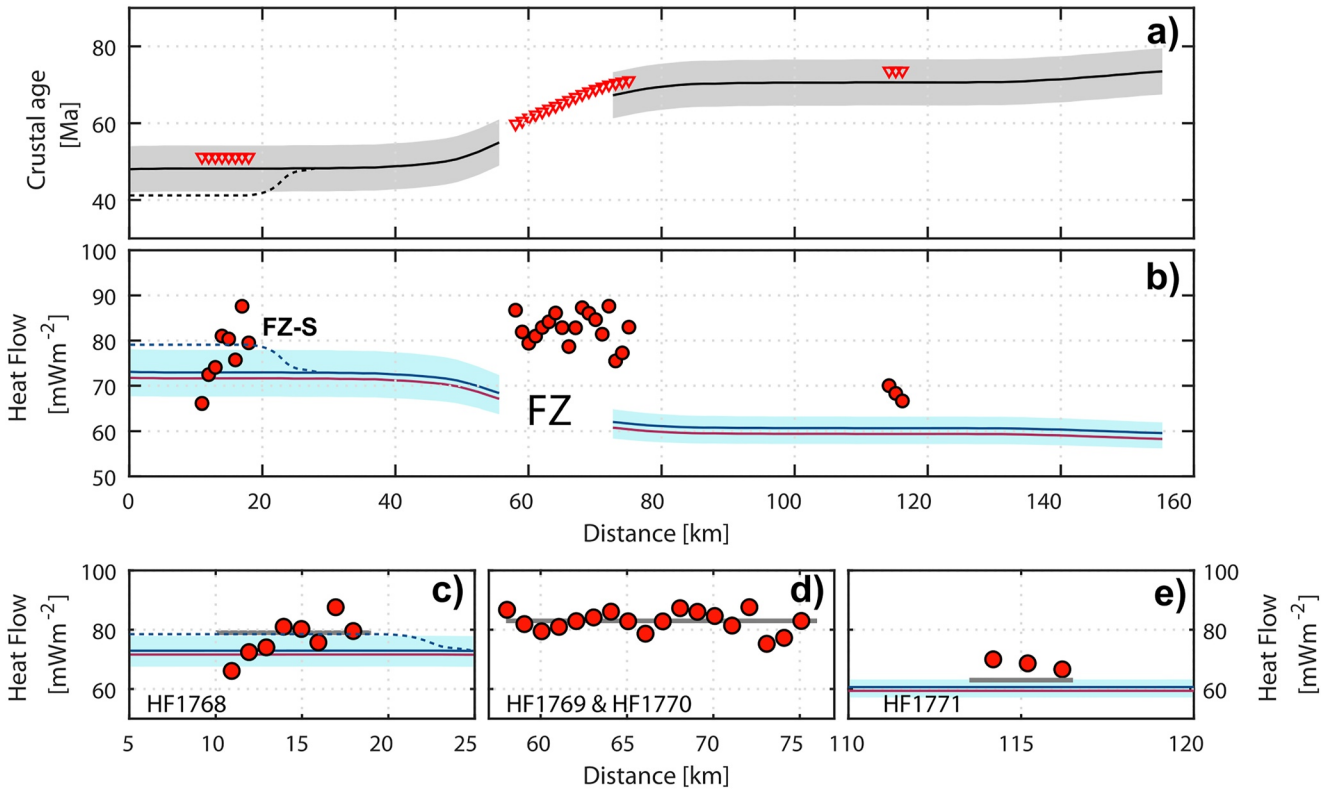

Figure 3. Heat flow with plate age. (a) Plate age along profile (black line—Müller et al., 2008) showing the age error of ±6 Ma (light gray). Heat flow measurement locations are shown as red inverted triangles. The suggested change in age due to the relocation of the St Paul fracture zone south (SPFZ-S) is shown by the black dashed line. (b) Predicted seafloor heat flow based on plate age from the plate cooling models of Hasterok (2013, blue solid line) and Mehouachi and Singh (2018, red solid line), with possible variation due to plate age errors shown in light blue. The change in predicted heat flow due to the relocation of the SPFZ-S (using the Hasterok, 2013, model) is shown by the blue dashed line. (c–e) Details from panel (b) for each heat flow site. The modeled basal heat flow is shown by the gray horizontal line.

of less than 1 mWm^{-2}. The largest misfit is within the St Paul FZ, which may be due to problems in correctly imaging the complex and steep basement topography used to create the model, and/or non-2D effects.

Compared with the predicted heat flow from conductive plate cooling models (Figure 3), the modeled basal heat flow to the north of St Paul (site HF1771) fits well (63 modeled versus ~62 mWm^{-2} predicted), suggesting a purely conductive cooling regime at this site. To the south of St Paul (site HF1768), modeled basal heat flow is ~6 mWm^{-2} higher than that predicted from the plate cooling model, using the plate age from the global age model (79 modeled versus ~73 mWm^{-2} predicted). The modeled value is only 1 mWm^{-2} outside the predicted value error bounds of 68–78 mWm^{-2}, which are dependent on errors in plate age of ±6 Ma (after Müller et al., 2008). If we instead use our suggested age of 41 Ma for the southern site, the predicted heat flow becomes 79 mWm^{-2}, equal to the modeled value. This supports the relocation of the second FZ to 1°34′N and suggests that the heat flow regime is purely conductive to the south of St Paul. Within the FZ itself (site HF1769/HF1770), the plate age and therefore predicted heat flow is not well constrained but is expected to lie between the values to the north (62 mWm^{-2}) and south (73 mWm^{-2}) of the SPFZ-N, with an average value of 68 mWm^{-2} assuming a linear age variation. However, we observe a modeled basal heat flow of 83 mWm^{-2}, much higher than the predicted and observed values on both sides of the FZ valley. Thus, we have a positive heat flow anomaly of 10–15 mWm^{-2} compared to the conductive cooling models, suggesting that other processes must be influencing the heat flow and thermal structure within the FZ valley.

The seismic reflection profile and co-located sub-bottom profile provide both large-scale and shallow, high-resolution images, respectively, of the sediments within the FZ valley (Figure 4). Sediments are expected to comprise typical abyssal plain nannofossil oozes and pelagic clays (Ruddiman et al., 1988). The seismic image (Figure 4a) shows evidence of normal faulting throughout the lifetime of the FZ, which could be related

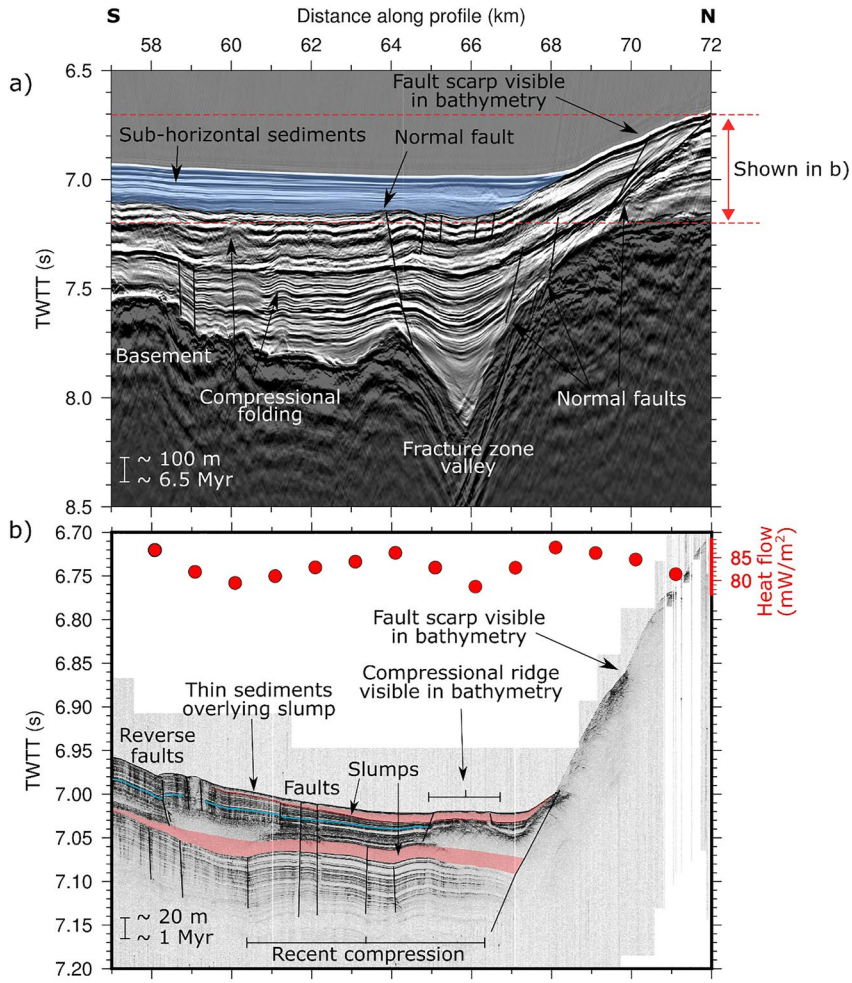

Figure 4. Images of the sediment within the St Paul fracture zone (FZ). (a) Seismic reflection section (Mehouachi & Singh, 2018) of the sediments, with the basement shaded in dark gray. Deformation is indicated by faulting (black lines), some of which is recent enough to offset the top layer of sediment on the northern valley wall, and minor folding. Within the FZ valley most deformation likely occurred before the deposition of the relatively undisturbed, sub-horizontal sediment package (blue shaded). Red dashed lines indicate the range of TWTT shown in panel (b). (b) Sub-bottom profiler section, showing recent compression in the uppermost sediments forming folds and reverse faults (offset shown by reflector highlighted in blue). Two acoustically transparent slump layers (pale red shaded) suggest recent tectonic movement destabilizing the northern valley wall. Black lines are faults and the positions and values of heat flow measurements from site HF1769/1770 are shown in red circles.

to sediment compaction, as well as some compressional deformation through sediment folding. A ∼170 m-thick, relatively undeformed top package of sub-horizontal sediments suggests the last significant deformation occurred at ∼7–11 Ma, assuming sedimentation rates of 15–22 m/Ma (Ruddiman et al., 1988). However, the sub-bottom profiler image of the upper ∼100 m of sediments shows small-scale deformation occurring until very recently (Figure 4b). Two acoustically transparent layers which thin to the south are likely recent slump events from the northern valley wall, estimated to be ∼9 and ∼13 m thick and to have occurred 100–200 ka and 1.5–2.0 Ma, respectively. Evidence for compression is also indicated by folding of the sediments and reverse faults offsetting the seabed with a throw up to ∼9 m.

4. Discussion

The observed heat flow anomaly of 10–15 mWm^{-2} within the St Paul FZ is a significant deviation from the predicted conductive values, and the basal value (83 mWm^{-2}) represents the maximum heat flow measured to date between the bounding MAR ridge segments and the coast of Africa. Nearby measurements within a 400 km

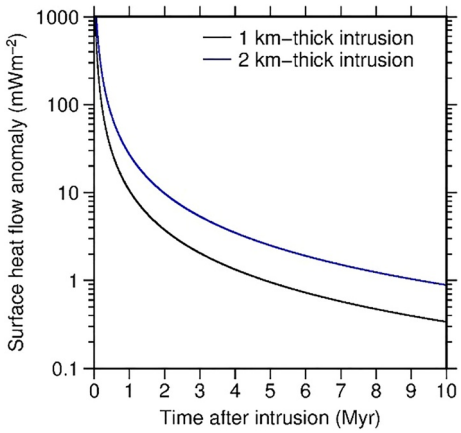

Figure 5. Surface heat flow anomaly caused by melt intrusion against time. Modeling of the heat flow from oceanic lithosphere after the intrusion of 1 and 2 km thick melt intrusions shows surface heat flow returns to within 1 mWm^{-2} of normal values within 10 Myr. The large thicknesses were chosen to simulate an end-member scenario with the maximum effect on surface heat flow.

radius of our profile have a maximum value of 75 mWm^{-2} and an average of 65 mWm^{-2} (Herman et al., 1977; Vacquier & von Herzen, 1964; von Herzen & Simmons, 1972), similar to our observations north and south of the St Paul FZ.

We consider several possible processes which could influence the heat flow within the FZ or explain the observed positive anomaly: (a) mantle thermal anomalies; (b) thermal rejuvenation of the lithosphere and crustal thickening at the ridge-transform intersection; (c) alteration or production of heat within the FZ; and (d) hydrothermal flow.

4.1. Mantle Thermal Anomalies

The influence of the nearby Sierra Leone mantle plume along with the proposed equatorial Atlantic mantle "cold spot" (Schilling, 1995) could affect the heat flow of the study area. The effects of these mantle domains can be seen in the bathymetry and basement depth across the St Paul TF and FZ and the adjacent ridge segments, with the warming influence of the mantle plume shallowing the northern MAR segment by ∼300 m compared to the segment south of St Paul. This trend of shallower bathymetry continues along the FZ to our study area. If we assume that the ridge to the north and the south of the FZ had the same depth at the time of formation, we would expect the northern basement to be ∼260 m deeper from plate cooling models. However, after correcting for sediment loading (Sykes, 1996), it is only ∼20 m deeper than the basement depth to the south. Despite this bathymetric effect, the fact that the observed basal heat flow to the north of St Paul matches the predicted values well suggests that, although the mantle regimes may have influenced the bathymetry of the ridge axis, they have had little effect on the surface heat flow of the older lithosphere.

4.2. Thermal Rejuvenation of the Crust

The thermal age of the seafloor used to calculate predicted heat flow is derived from the simple geometry of the ridge-transform system, however, this, and the use of standard plate cooling models (e.g., Hasterok, 2013; Stein & Stein, 1992), may not be appropriate. These methods assume that the heat flow within the FZ should, in a normal case, be between the heat flow exhibited by the lithosphere on either side, and should display a similar thermal structure at formation and subsequent thermal evolution with age. However, these cooling models predict a colder temperature structure than more advanced thermal models of TFs (Behn et al., 2007; Grevemeyer et al., 2021; Wang et al., 2022), which may take into account, for example, mantle upwelling from extensional stresses. We note that these effects are greatest in the center of the TF, and thermal structure should return to levels more similar to plate cooling models closer to the fault ends where the FZ begins. Furthermore, it has recently been proposed that TF crust, and therefore FZ crust, forms in a two-stage accretion process involving initial magmatic accretion at one spreading center, a period of stretching and extension along the TF, before another period of heating and magmatism at the opposite RTI where the two plates are welded together to form the FZ (Grevemeyer et al., 2021). Bathymetric studies have shown evidence in the form of J-shaped ridges for this lateral movement of melt at RTIs from the ridge axis into the TF and even penetrating into the older plate (Grevemeyer et al., 2021; Marjanović et al., 2020). These J-shaped ridges have also been observed at the St Paul FZ in the vicinity of our study area (Growe et al., 2021). This addition of heat and/or melt at the RTI could increase the temperature of the lithosphere, effectively making the lithosphere appear thermally "younger" than its true age when observing its heat flow.

To investigate the effect of melt injection at the RTI, we modeled the intrusion and cooling of a melt sill in a 1D geotherm profile representing the oceanic lithosphere opposite the RTI. After 10 Myr, both a 1 km-thick and 2 km-thick sill inserted into the oceanic crust at a depth of 1 km below surface produce a surface heat flow anomaly of under 1 mWm^{-2} (Figure 5). This modeling did not take into account lateral conduction or warming at the RTI, for example, through mantle upwelling, however, thermal models provide little evidence for the significant passive transfer of heat at RTIs (e.g., Roland et al., 2010).

We also note that even if lateral conduction or melt injection at the RTI increases the temperature within the FZ, it should not increase the heat flow to greater than that of the adjacent newly formed crust at the ridge axis, which is what we observe around the St Paul FZ with a higher basal heat flow within the FZ than that of the adjacent younger crust. Even if the thermal age of the lithosphere was reset to the same age as the younger lithosphere, this would predict a heat flow of 73 mWm^{-2}, compared to the observed value of 83 mWm^{-2}. Using simple 2D analytical plate cooling models, we calculate that the thermal age would need to be reset by an average of ∼11–20 Myr to match the observed heat flow anomaly. In terms of lithospheric thickness, the nascent FZ lithosphere at the RTI would require thinning from a thickness of 32–45 km to a maximum of ∼9.5 km, and a minimum value of thinner than the lithosphere at the adjacent ridge axis, taking the 1260°C isotherm to represent the base of the lithosphere. This would require the heating of the original LAB to mantle potential temperatures (e.g., 1360°C). Therefore, although there is evidence for the addition of melt to the FZ crust when it was at the RTI, we do not consider that thermal rejuvenation can likely explain the observed heat flow anomaly at St Paul, or, at least, the whole of the observed anomaly. Thermal rejuvenation could, however, significantly influence heat flow measurements much closer to the RTI (within ∼1 Myr of passing the intersection) if considerable amounts of melt are added to the crust.

4.3. Near-Surface Disturbances or Production of Heat Within the FZ

Here, we first consider the possibility that the slumping events observed in the upper sediment package (Figure 4b) may have disturbed the thermal structure and hence temperature gradients. In general, rapid sedimentation lowers the temperature gradient in the deposited sediments (Wangen, 2010), which would mean that the undisturbed steady state temperature gradients are higher than those measured. Modeling the equilibrium process of the uppermost slump shows that a 100–200 ka, 10 m-thick slump would have equilibrated to within a few percent of the undisturbed temperature profile within this time period, with any remaining effects below the temperature resolution of 1 mK of the heat probe.

We next consider several possible sources of heat within the FZ. Radioactive decay is the main source of heat production within the Earth, however, inputting realistic production values of up to 1 μWm^{-3} for sediments and lithosphere into numerical models cannot explain the observed anomaly within the FZ, as production is not expected to be higher there than outside the FZ. Alternatively, at slow-spreading ridge environments the exothermic reaction between seawater and mantle peridotite has been shown to produce enough heat to drive low-temperature hydrothermal systems (Früh-Green et al., 2003), and some TFs and FZs have been shown to consist of significant amounts of exhumed peridotite (e.g., Cannat et al., 1991; Gregory et al., 2021). However, a recent tomographic study across our heat flow profile (Growe et al., 2021) does not indicate the presence of meaningful amounts of exhumed or serpentinized peridotite, and the thick sediment cover with a very low permeability (Spinelli et al., 2004) would inhibit the penetration of enough seawater to produce significant hydration of the igneous basement.

Finally, we consider the production of heat through deformation. Although FZs are assumed to be inactive, intraplate discontinuities, they have been observed to host significant global earthquakes (e.g., Robinson, 2011), including a Mb 5.2 event in the Chain FZ, ∼400 km south of St Paul, in 2016 (USGS, 2020). These observations suggest that multiple smaller events, undetectable by land-based global seismometer networks, may occur on FZs. A study of different sites along the Vema FZ found evidence of tectonic activity in crust up to ∼109 Ma (Devey et al., 2018). The analysis of the sediment images (Figure 4) from the St Paul FZ shows minor deformation occurring throughout the lifetime of the FZ up until the present day, both in compressional and extensional senses, as a pure strike-slip movement is difficult to observe due to the orientation of the profile. Recent movement is also visible in discontinuities in the sediment cover and slope changes in the seafloor seen in the bathymetry data along the FZ, suggesting some extensional movement in the northern FZ wall and compressional behavior in the FZ valley (Figure 6). This deformation could be caused by intraplate stress due to regional plate directional changes ∼11 Ma (Maia et al., 2016), which are responsible for a number of significant bathymetric features at the St Paul TF and the wider equatorial Atlantic region (Bonatti et al., 1994, 2005), including the 4.5 km-high Romanche transform ridge located only ∼150 km to the south of the study area. This plate motion reorganization event may have caused the last major deformation visible in the seismic image, which is estimated to have occurred ∼7–11 Ma (Figure 4a). Furthermore, global bathymetric and gravity data show that the St Paul TF system has evolved from a two-fault system active until ∼20 Ma to a more complex

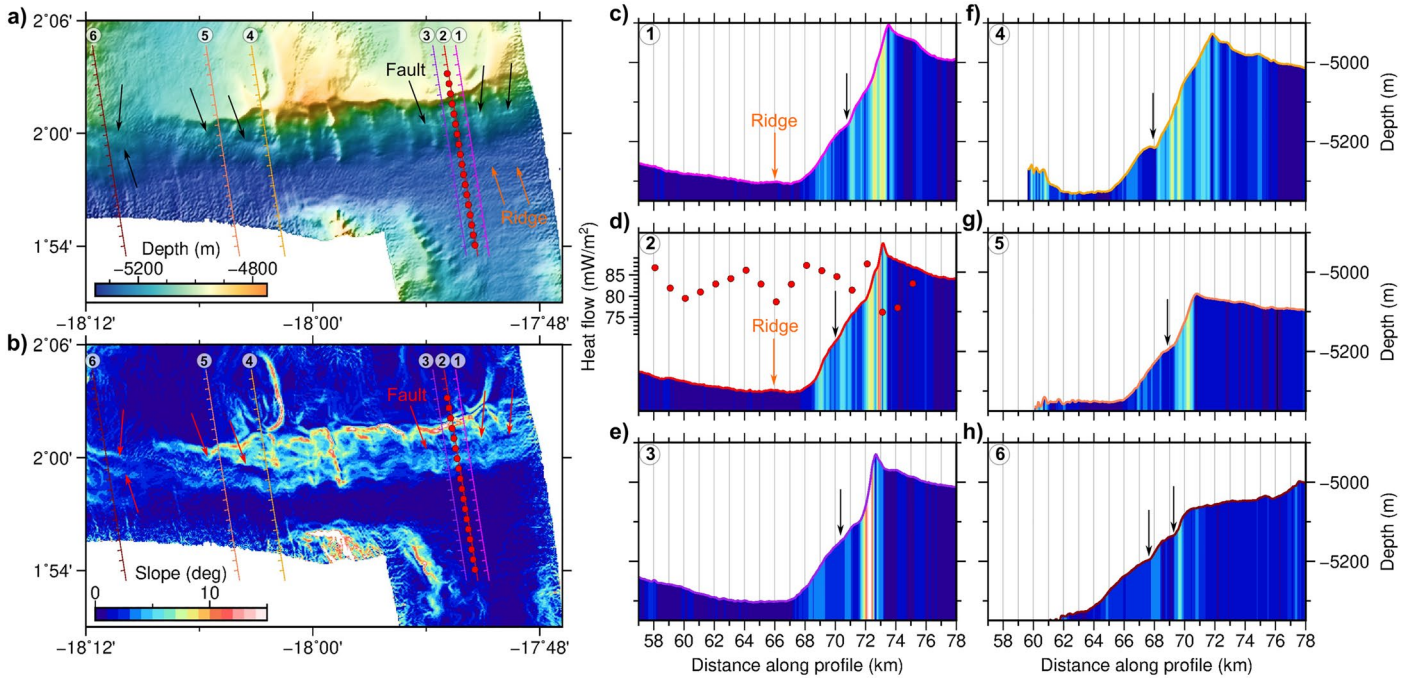

Figure 6. Detailed bathymetry of the St Paul fracture zone. (a) Multibeam swath bathymetry showing the fracture zone (FZ) valley and heat flow measurement positions from site HF1769/1770 (red circles). Linear breaks in the sediment surface suggest recent tectonic movement or faulting (indicated by black arrows), and small positive seafloor structures may indicate recent compression forming small ridges (indicated by orange arrows). Numbered colored lines indicate bathymetric profiles shown in panels (c–h), with tick marks every 1 km. These features suggest recent tectonic activity is not limited to along the heat flow profile but extends further along the FZ. (b) Seafloor slope calculated from the bathymetry data, highlighting changes in slope where faults (red arrows) have been identified. (c–h) Bathymetric profiles across the FZ, colored by slope below the plotted seafloor line. Seafloor line color corresponds to the profile color in panels (a) and (b). Features indicating recent tectonic movement identified in the map view are shown here by black arrows (faults) or orange arrows (ridges). Profile 2 shown in panel (d) is coincident with the heat flow profile, and the locations and values of the measurements are shown by red circles. The faults and ridges identified along this profile are also visible in the seismic and/or sub-bottom profiler images (Figure 4).

configuration consisting of four faults separating three small intra-transform spreading segments, widening from ~50 km at our study area to >80 km at present day. This evolution may also have caused some intraplate stresses. Additionally, it has previously been proposed that the thermal differences across FZs, leading to different rates of subsidence across these features, can cause vertical dip-slip motion (De Long et al., 1977). At our heat flow profile, plate cooling models (Hasterok, 2013) would predict a contemporary dip-slip rate of 9 m/Ma (0.009 mm/a), with cumulative dip-slip of ~1,700 m since the welding of the FZ lithosphere at the eastern RTI to the present day. Furthermore, the active part of the 880 km-long Romanche TF is just 150 km south of our study, which has produced a 20 km-wide and 6,000 m-deep rift valley, and might have induced compressional stress along the St Paul FZ.

To quantify the amount of heat that may be produced by deformation, we use the formula of Leloup et al. (1999) to calculate shear heating, before using a numerical model to determine the resulting surface heat flow contribution. Using a friction coefficient on the order of 0.5 (Byerlee, 1978) and restricting shear heating to the brittle zone (down to 600°C—upper ~20 km), a 10-km wide zone of shear heating with a steady-state slip rate of 2–3 mm/a is required to produce a heat flow anomaly of 10–15 mWm^{-2}. This is a generous estimate of the friction coefficient, which could be lower in the fault zone (England, 2018; Fulton et al., 2013; Leloup et al., 1999), resulting in less heat being produced for the same width and slip rate. The result of 2–3 mm/a of slip is a relatively high value that should produce larger, globally observed earthquakes, and subsequently large offsets in bathymetric features, neither of which are observed. If this slip is represented by strike-slip motion along the FZ, it would be similar to observed slip-rates along FZs in the Wharton Basin that have resulted in large ($M > 8$) earthquakes (Coudurier-Curveur et al., 2020). Furthermore, models of the thermal regime in active TFs have suggested that shear heating has a minimal final effect on the thermal structure (Roland et al., 2010). Therefore, we do not consider that heat produced directly through different forms of deformation, including dip-slip, compression or strike-slip reactivation can explain the observed heat flow anomaly.

4.4. Hydrothermal Flow

Although we have explained that the observed deformation within the St Paul FZ is unlikely to be capable of generating significant amounts of heat, this tectonic activity could play a role in enabling or driving fluid circulation and therefore heat advection within the basement. Further to the deformation sources already proposed, different thermal contraction rates and lithospheric density across FZs result in flexural adjustment of the lithosphere in response to the resultant pressure gradients (Sandwell, 1984), which explains the persistent seafloor relief of FZs as they age. This adjustment steepens the relief of the FZ valleys, which may be the cause of the slumping events and some of the deformation seen in the sedimentary sections. Together, these sources of deformation may create fluid pathways within the crust, as well as influencing pressure gradients, which could drive fluid flow. Tomographic studies of TFs have found velocity anomalies interpreted to represent high amounts of fracturing and porosity within the basement (Gregory et al., 2021; Roland et al., 2012). Although this porosity is likely to be reduced over time and may be affected by crustal thickening at the RTI (Grevemeyer et al., 2021; Marjanović et al., 2020), at the St Paul FZ the slightly reduced velocities within the fault zone suggest a porosity increase as compared to the adjacent crust (Growe et al., 2021). Porosity is predicted to be on the order of ∼16% in the top basement rocks, decreasing to ∼5% at 1 km and ∼2% at 2 km below the sediment-basement interface (Growe et al., 2021). Although the relationship between porosity and permeability within the oceanic crust is complex, it is likely that the uppermost 1 km represents a more permeable layer due to its increased porosity, which could enable fluid flow.

Due to the extensive low permeability sediment cover, we do not expect well-ventilated fluid flow, but lateral or vertical circulation within the basement which may be advecting heat into the FZ, such as that observed in other off-axis areas (e.g., Fisher & Von Herzen, 2005). Previous studies at the Vema FZ (Devey et al., 2018) and Southwest Iberian Margin strike-slip faults (Hensen et al., 2022) found evidence for active fluid flow within sedimented seafloor. Our modeling results showed that the small-scale heat flow variation within the FZ can be satisfactorily explained through conductive refraction from changes in the basement and seafloor topography (Figure 2), and does not require very local, shallow heat advection (Fisher & Von Herzen, 2005). Instead, the fluid circulation is required to produce the 10–15 mWm^{-2} anomaly observed across the FZ valley, which is at least 17 km-wide. We interpret these observations to suggest the presence of larger-scale, deeper hydrothermal circulation within the upper crust, with strong flow channeling controlled by the permeability structure preventing the formation of small-scale convection cells at the basement surface (Fisher & Becker, 2000). The lack of an observed heat flow low either to the north or south of the FZ likely precludes lateral advection across the FZ, unless the circulation cell size is smaller than the spacing between our measurement sites of 50 km, thus we envisage either east-west lateral advection along the FZ, or vertical flow.

If we assume that the conductive contribution to the heat flow within the FZ is as predicted through plate cooling (Hasterok, 2013), we can estimate the vigor of the fluid circulation through calculation of the Nusselt number (Nu), representing the ratio of total heat flow to purely conducted heat (Becker & Davis, 2004). Using a predicted conducted heat flow of 68 mWm^{-2} and the modeled total basal heat flow of 83 mWm^{-2}, we estimate the value of Nu as ∼1.2. We can then use Nu to estimate the Rayleigh number (Ra), which indicates both whether convection is able to take place and whether it is steady state. Following the relationships detailed in Wang (2004—Equation 12.24) we find that Ra could be up to ∼50. This is greater than the general critical Ra value for enabling convection within oceanic crust (∼40) (Becker & Davis, 2004), which is likely to be lower in our case due to the significant topography within the FZ that would encourage convection, but relatively low in general, suggesting that convection is present but is limited. Assuming typical values for the physical properties of the oceanic crust and circulating seawater, and a Ra value of 50, we can use Equation 1 (Wang & Davis, 2003) to estimate the permeability of the crust for different convective layer thicknesses.

$$\mathbf{Ra} = \frac{\kappa \rho^2 c \varnothing g h \Delta T}{k \mu} \tag{1}$$

Where $\boldsymbol{\kappa}$ is the permeability, $\boldsymbol{h}$ is the layer thickness and $\boldsymbol{\Delta T}$ is the temperature difference across it, $\boldsymbol{k}$ is the thermal conductivity of the basement (here we use 2 $Wm^{-1}K^{-1}$), and $\boldsymbol{\rho}$, $\boldsymbol{c}$, Ø, and $\boldsymbol{\mu}$ are the density, specific heat, thermal expansion coefficient, and dynamic viscosity of water, respectively. For each permeability value we varied the layer thickness by 100 m until the difference between the calculated $\boldsymbol{\Delta T}$ and the temperature difference predicted by the plate cooling model was at a minimum, with the results shown in Table 3.

Table 3
Results of Permeability Analysis for Basement Circulation

Permeability (m^2)	Layer thickness (m)	ΔT (°C)	Predicted ΔT from cooling models (°C)
10^{-10}	100	2.4	1.9
10^{-11}	400	6.1	7.7
10^{-12}	1,100	22.1	21
10^{-13}	3,500	69.3	66.9

As the porosity increase of the crust at St Paul is estimated to be greatest within the uppermost ~1 km (Growe et al., 2021), we consider a layer thickness of 400–1,100 m and corresponding permeability of 10^{-11}–10^{-12} m^2 to be the most likely. These calculations suggest that the permeability of the upper crust within the St Paul FZ could be reasonably high, compared to the wide possible range of permeability for oceanic crust, from as high as 10^{-9} m^2 for the uppermost 100 m (Davis et al., 2004) to as low as 10^{-22} m^2 calculated from core samples (Fisher, 1998). The upper crust in this location has been shown to likely comprise of extrusive basalts (Growe et al., 2021), which is consistent with the suggested permeability. For example, a permeability of 10^{-12} m^2 is similar to that proposed for the top 1 km of the crust at 13°N on the East Pacific Rise (Evans, 1994), and also within the ranges predicted for sedimented, relatively old crust (Fisher & Becker, 2000).

At the St Paul FZ, the observed high heat flow, flanked by conductive regimes to the north and south, suggests that the FZ could act as a higher permeability channel within the lithosphere as compared to the adjacent crust. In general, significant hydrothermal circulation within the oceanic lithosphere is expected to end at an age of ~65 Ma, due to increased sedimentation and a reduction in permeability and lithospheric heat with age (Stein & Stein, 1994). Crust with >400 m of sediment cover can have a "sealing age" of as young as 25 Ma, which may explain why both the lithosphere to the north and south of the FZ, aged ~71 Ma and ~48 Ma, respectively, exhibit conductive heat flow regimes indicative of no heat advection. Increased permeability within the FZ itself could be due to the more intensely fractured fabric inherited from the TF regime, which would form a preferential pathway for fluid as a channelized flow system (e.g., Fisher & Becker, 2000). The continuing minor tectonic activity may aid the higher permeability to persist over time. This excess permeability, coupled with buoyancy forces, could be sufficient to maintain fluid flow. However, circulation could be further encouraged by the significant seafloor topography, pressure gradients, and lithospheric flexure present at the FZ. This likely results in greater pressure gradients than in normal ridge-flank crust, which may be limited to temperature or buoyancy-driven flow (Fisher & Becker, 2000). Thus, the FZ could behave as a vertical conduit for fluid flux, with the width of the observed anomaly at the surface related to the width of the conduit, or it could enable transient flow along the fault (e.g., Wang, 2004). Upwelling fluid flow could be further encouraged due to the warming effect of the thick sedimentary section within the FZ valley (Davis & Becker, 2004).

4.5. Do Fracture Zones Have an Inherently Different Thermal Structure to Normal Oceanic Crust?

Throughout this paper, we have compared the observed heat flow at the St Paul FZ with predicted values from plate cooling models, assuming that the heat flow within the FZ should, in a normal case, be between the heat flow exhibited by the lithosphere on either side. However, as discussed previously, FZ crust may have a different formation mechanism involving rejuvenation at the RTI, and therefore thermal structure and evolution to ordinary oceanic lithosphere (e.g., Grevemeyer et al., 2021). Furthermore, a deep low velocity anomaly imaged at the Romanche TF (Wang et al., 2022) potentially suggests thinning of the lithosphere within the transform zone caused by deep hydration and water-induced melting. At the Romanche TF, the LAB shallows by ~15 km compared to the predicted thickness (i.e., the average thickness of the lithosphere on either side of the transform) or by ~6 km compared to the thinner, younger lithosphere. If we use plate cooling models and assume the top of the LAB occurs at a temperature of 1260°C (Mehouachi & Singh, 2018), this thinning would be equivalent to a decrease in age of ~2–12 Myr, in effect making the TF lithosphere appear "younger" than the lithosphere bounding the fault on both sides. Interestingly, this is what the observed heat flow indicates at St Paul, with the anomaly equivalent to an average age reset of ~11–20 Myr. Both of these recent studies therefore suggest that TF and FZ lithosphere may not be comparable to lithosphere formed at spreading centers, and the standard plate cooling models may not accurately predict the thermal regime in these locations.

Additional indications that FZ crust could be considered in a different class to "standard" oceanic crust include tomographic studies showing significant fracturing of transform crust at a variety of spreading rates (Gregory et al., 2021; Roland et al., 2012; Van Avendonk et al., 1998), which suggest FZs could have heightened permeability down to, and possibly below, the Moho. Also, seismic events have been observed to occur on FZs, such as an event on the Chain FZ in 2016 (USGS, 2020), indicating that some tectonic activity and deformation along

FZs may be widespread. The differential temperature and pressure forces which could drive this activity, as well as lithospheric flexure, are also expected to act at all FZs over their lifetime.

These new discoveries suggest that we could perhaps expect heat flow anomalies at all FZs, either as a result of differing initial temperature structure, and/or from advected heat through fluid flow as suggested for the St Paul FZ. The size of anomalies or extent of fluid flow could be related to parameters such as the size or age-offset of the FZ, which has been found to correlate with TF morphology (Ren et al., 2022). The St Paul FZ system has a total age-offset of 30 Myr and offset length of ~560 km (23 Myr and ~300 km for St Paul FZ-N only), compared to a global average offset of 40 km for oceanic TFs (Bird, 2003). It therefore represents a larger TF system which may exhibit more extreme differences in crustal formation, as well as greater differential stresses between the juxtaposed sections of lithosphere. At the location of the only other cross-FZ heat flow study (Kolandaivelu et al., 2017), the Ecuador FZ in the Pacific, the authors found anomalous heat flow and suggested significant fluid flow within the basement to explain the deficit, requiring a permeability of 10^{-12} m^2 for a 1,000 m-thick basement aquifer, which matches our estimated permeability for the St Paul FZ. The Ecuador FZ has a small age-contrast of 4.5 Myr, but the exposed basement outcrops on either side of the FZ valley could promote vigorous, ventilated fluid circulation without significant tectonic driving forces. An along-FZ and TF study at the Vema system found heat flow ranging from 66 to 170 mWm^{-2}, with an average of 124 mWm^{-2}, in the western FZ valley from the RTI to ~90 km along the FZ (Langseth & Hobart, 1976). Compared to conductive cooling estimates, these values give a spread of both positive and negative heat flow anomalies, suggestive of significant advection of heat. However, the lack of geophysical data allowing sediment thickness and basement topography to be mapped in the study area prevented full modeling of basement heat flow and heat advection. Similarly, within the global heat flow database (Lucazeau, 2019), there are only a few measurements made within TFs and FZs. These data provide very scattered values suggesting both positive and negative heat flow anomalies, but as they are often isolated measurements with little-to-no information about sediment thickness, basement topography, or heat flow on either side of the FZ, it is not possible to compare these data effectively with the St Paul results. Further comprehensive heat flow studies across both TFs and FZs are needed to fully investigate this hypothesis.

5. Conclusions

We have observed a positive 10–15 mWm^{-2} heat flow anomaly within the SPFZ, when compared to conductive cooling models, as well as evidence for continuous deformation within the FZ valley. After considering the possible causes for the anomaly, we conclude:

- The most likely cause for the anomaly is heat advected by fluid flow within a confined basement, with a potential basement permeability of 10^{-12} m^2, assuming a 1,000 m-thick permeable layer representing the basaltic upper crust.
- The large age-offset of the FZ and recent regional tectonic stress help to drive the fluid flow, creating an ideal, higher permeability environment to channel substantial, though not vigorous, basement fluid flow.
- We cannot discount possible contribution to the heat flow anomaly from thermal rejuvenation at the RTI, or from a different temperature structure within FZs caused by their different formation mechanism.
- FZ lithosphere could therefore need to be regarded differently to standard oceanic lithosphere formed at the spreading center when considering its structure, evolution with age, and ability to host hydrothermal circulation.

Data Availability Statement

The bathymetric grid shown in Figure 1b and the Parasound data (Figure 4b) can be downloaded from Pangaea (https://doi.pangaea.de/10.1594/PANGAEA.950419 and https://doi.pangaea.de/10.1594/PANGAEA.950420).

Acknowledgments
We thank the captain and crew of the RV Maria S. Merian and the scientific party for their excellent support during cruise MSM69, alongside Ingo Grevemeyer for his input as chief scientist. The funding of the cruise was provided by the German Science Foundation (DFG). The IPGP group has received funding from the European Research Council under the European Union's Seventh Framework Programme (FP7/2007–2013)/ERC Advance Grant 339442_TransAtlanticILAB to S.C. Singh. We thank Chris Harbord for useful discussions on heat produced by active faulting, and Robert Harris and Tao Zhang for their constructive comments which improved the manuscript. Figures were prepared using GMT (Wessel et al., 2013). This is IPGP publication number 4272. Open Access funding enabled and organized by Projekt DEAL.

References

Becker, K., & Davis, E. E. (2004). In situ determinations of the permeability of the igneous oceanic crust. In E. E. Davis & H. Elderfield (Eds.), *Hydrogeology of the oceanic lithosphere* (pp. 189–224). Cambridge University Press.

Behn, M. D., Boettcher, M. S., & Hirth, G. (2007). Thermal structure of oceanic transform faults. *Geology*, *35*(4), 307. https://doi.org/10.1130/G23112A.1

Bird, P. (2003). An updated digital model of plate boundaries. *Geochemistry, Geophysics, Geosystems*, *4*(3), 1–52. https://doi.org/10.1029/2001GC000252

Bonatti, E., Brunelli, D., Buck, W. R., Cipriani, A., Fabretti, P., Ferrante, V., et al. (2005). Flexural uplift of a lithospheric slab near the Vema transform (Central Atlantic): Timing and mechanisms. *Earth and Planetary Science Letters*, *240*(3–4), 642–655. https://doi.org/10.1016/j.epsl.2005.10.010

Bonatti, E., Ligi, M., Gasperini, L., Peyve, A., Raznitsin, Y., & Chen, Y. J. (1994). Transform migration and vertical tectonics at the Romanche fracture zone, equatorial Atlantic. *Journal of Geophysical Research*, *99*(B11), 21779–21802. https://doi.org/10.1029/94JB01178

Byerlee, J. (1978). Friction of rocks. *Pure and Applied Geophysics*, *116*(4–5), 615–626. https://doi.org/10.1007/BF00876528

Cannat, M., Mamaloukas-Frangoulis, V., Auzende, J.-M., Bideau, D., Bonatti, E., Honnorez, J., et al. (1991). A geological cross-section of the Vema fracture zone transverse ridge, Atlantic Ocean. *Journal of Geodynamics*, *13*(4), 97–118. https://doi.org/10.1016/0264-3707(91)90034-c

Christeson, G. L., Morgan, S., Kodaira, S., Yamashita, M., Almeev, R. R., Michibayashi, K., et al. (2016). Physical properties and seismic structure of Izu-Bonin-Mariana fore-arc crust: Results from IODP Expedition 352 and comparison with oceanic crust. *Geochemistry, Geophysics, Geosystems*, *17*(12), 4973–4991. https://doi.org/10.1002/2016GC006638

Coudurier-Curveur, A., Karakaş, Ç., Singh, S., Tapponnier, P., & Hananto, N. (2020). Is there a nascent plate boundary in the northern Indian Ocean? *Geophysical Research Letters*, *47*(7), e2020GL087362. https://doi.org/10.1029/2020GL087362

Davis, E. E., & Becker, K. (2004). Observations of temperature and pressure: Constraints on ocean crustal hydrologic state, properties, and flow. In E. E. Davis & H. Elderfield (Eds.), *Hydrogeology of the oceanic lithosphere* (pp. 225–271). Cambridge University Press.

Davis, E. E., Becker, K., & He, J. (2004). Costa Rica Rift revisited: Constraints on shallow and deep hydrothermal circulation in young oceanic crust. *Earth and Planetary Science Letters*, *222*(3–4), 863–879. https://doi.org/10.1016/j.epsl.2004.03.032

De Long, S. E., Dewey, J. F., & Fox, P. J. (1977). Displacement history of oceanic fracture zones. *Geology*, *5*(4), 199–202. https://doi.org/10.1130/0091-7613(1977)5<199:DHOOFZ>2.0.CO;2

Devey, C. W., Augustin, N., Brandt, A., Brenke, N., Köhler, J., Lins, L., et al. (2018). Habitat characterization of the Vema fracture zone and Puerto Rico trench. *Deep-Sea Research Part II Topical Studies in Oceanography*, *148*, 7–20. https://doi.org/10.1016/j.dsr2.2018.02.003

England, P. (2018). On shear stresses, temperatures, and the maximum magnitudes of earthquakes at convergent plate boundaries. *Journal of Geophysical Research: Solid Earth*, *123*, 7165–7202. https://doi.org/10.1029/2018JB015907

Evans, R. L. (1994). Constraints on the large-scale porosity and permeability structure of young oceanic crust from velocity and resistivity data. *Geophysical Journal International*, *119*(3), 869–879. https://doi.org/10.1111/j.1365-246X.1994.tb04023.x

Fisher, A. T. (1998). Permeability within basaltic oceanic crust. *Reviews of Geophysics*, *36*(2), 143–182. https://doi.org/10.1029/97RG02916

Fisher, A. T., & Becker, K. (2000). Channelized fluid flow in oceanic crust reconciles heat-flow and permeability data. *Nature*, *403*(6765), 71–74. https://doi.org/10.1038/47463

Fisher, A. T., & Von Herzen, R. P. (2005). Models of hydrothermal circulation within 106 Ma seafloor: Constraints on the vigor of fluid circulation and crustal properties, below the Madeira Abyssal Plain. *Geochemistry, Geophysics, Geosystems*, *6*(11), Q11001. https://doi.org/10.1029/2005GC001013

Früh-Green, G. L., Kelley, D. S., Bernasconi, S. M., Karson, J. A., Ludwig, K. A., Butterfield, D. A., et al. (2003). 30,000 Years of hydrothermal activity at the Lost City vent field. *Science*, *301*(5632), 495–498. https://doi.org/10.1126/science.1085582

Fulton, P. M., Brodsky, E. E., Kano, Y., Mori, J., Chester, F., Ishikawa, T., et al. (2013). Low coseismic friction on the Tohoku-Oki fault determined from temperature measurements. *Science*, *342*(6163), 1214–1217. https://doi.org/10.1126/science.1243641

GEBCO Compilation Group. (2019). GEBCO 2019 grid. https://doi.org/10.5285/836f016a-33be-6ddc-e053-6c86abc0788e

Gregory, E. P. M., Singh, S. C., Marjanović, M., & Wang, Z. (2021). Serpentinized peridotite versus thick mafic crust at the Romanche oceanic transform fault. *Geology*, *49*(9), 1132–1136. https://doi.org/10.1130/G49097.1

Grevemeyer, I., Rüpke, L. H., Morgan, J. P., Iyer, K., & Devey, C. W. (2021). Extensional tectonics and two-stage crustal accretion at oceanic transform faults. *Nature*, *591*(7850), 402–407. https://doi.org/10.1038/s41586-021-03278-9

Grevemeyer, I., Singh, S., Villinger, H., Papenberg, C., & Kaul, N. (2019). LITHOS-iLAB–structure and evolution of the oceanic lithosphere, cruise No. MSM69, 14.11.2017–22.12.2017, Mindelo/Praia (Cape Verdes)–Mindelo (Cape Verdes). In *MARIA S. MERIAN-Berichte*, (Vol. MSM69, pp. 1–62). Gutachterpanel Forschungsschiffe. https://doi.org/10.2312/cr_msm69

Growe, K., Grevemeyer, I., Singh, S. C., Marjanović, M., Gregory, E. P. M., Papenberg, C., et al. (2021). Seismic structure of the St. Paul fracture zone and late cretaceous to mid-Eocene oceanic crust in the equatorial Atlantic Ocean near 18°W. *Journal of Geophysical Research: Solid Earth*, *126*(11), e2021JB022456. https://doi.org/10.1029/2021JB022456

Hartmann, A., & Villinger, H. (2002). Inversion of marine heat flow measurements by expansion of the temperature decay function. *Geophysical Journal International*, *148*(3), 628–636. https://doi.org/10.1046/j.1365-246x.2002.01600.x

Hasterok, D. (2013). A heat flow based cooling model for tectonic plates. *Earth and Planetary Science Letters*, *361*, 34–43. https://doi.org/10.1016/j.epsl.2012.10.036

Hensen, C., Duarte, J. C., Vannucchi, P., Mazzini, A., Lever, M. A., Terrinha, P., et al. (2019). Marine transform faults and fracture zones: A joint perspective integrating seismicity, fluid flow and life. *Frontiers of Earth Science*, *7*, 39. https://doi.org/10.3389/feart.2019.00039

Hensen, C., Scholz, F., Liebetrau, V., Kaul, N., Nuzzo, M., Schmidt, M., et al. (2022). Oceanic strike-slip faults represent active fluid conduits in the abyssal sub-seafloor. *Geology*, *50*(2), 189–193. https://doi.org/10.1130/g49344.1

Herman, B. M., Langseth, M. G., & Hobart, M. A. (1977). Heat flow in the oceanic crust bounding western Africa. *Tectonophysics*, *41*(1–3), 61–77. https://doi.org/10.1016/0040-1951(77)90180-9

Hyndman, R. D., Davis, E. E., & Wright, J. A. (1979). The measurement of marine geothermal heat flow by a multi penetration probe with digital acoustic telemetry and in situ thermal conductivity. *Marine Geophysical Researches*, *4*(2), 181–205. https://doi.org/10.1007/bf00286404

International Heat Flow Commission. (2012). Global heat flow database. In *The global heat flow database of the International Heat Flow Commission (IHFC)*. University of North Dakota. Retrieved from http://ihfc-iugg.org/products/global-heat-flow-database

Kohli, A., Wolfson-Schwehr, M., Prigent, C., & Warren, J. M. (2021). Oceanic transform fault seismicity and slip mode influenced by seawater infiltration. *Nature Geoscience*, *14*(8), 606–611. https://doi.org/10.1038/s41561-021-00778-1

Kolandaivelu, K. P., Harris, R. N., Lowell, R. P., Alhamad, A., Gregory, E. P. M., & Hobbs, R. W. (2017). Analysis of a conductive heat flow profile in the Ecuador fracture zone. *Earth and Planetary Science Letters*, *467*, 120–127. https://doi.org/10.1016/J.EPSL.2017.03.024

Langseth, M. G., & Hobart, M. A. (1976). Interpretation of heat flow measurements in the Vema fracture zone. *Geophysical Research Letters*, *3*(5), 241–244. https://doi.org/10.1029/gl003i005p00241

Leloup, P. H., Ricard, Y., Battaglia, J., & Lacassin, R. (1999). Shear heating in continental strike-slip shear zones: Model and field examples. *Geophysical Journal International*, *136*(1), 19–40. https://doi.org/10.1046/j.1365-246X.1999.00683.x

Lister, C. R. B. (1979). The pulse probe method of conductivity measurement. *Geophysical Journal of the Royal Astronomical Society*, *57*(2), 451–461. https://doi.org/10.1111/j.1365-246x.1979.tb04788.x

Lucazeau, F. (2019). Analysis and mapping of an updated terrestrial heat flow data set. *Geochemistry, Geophysics, Geosystems*, *20*(8), 4001–4024. https://doi.org/10.1029/2019GC008389

Maia, M., Sichel, S., Briais, A., Brunelli, D., Ligi, M., Ferreira, N., et al. (2016). Extreme mantle uplift and exhumation along a transpressive transform fault. *Nature Geoscience*, *9*(8), 619–623. https://doi.org/10.1038/ngeo2759

Marjanović, M., Singh, S. C., Gregory, E. P. M., Grevemeyer, I., Growe, K., Wang, Z., et al. (2020). Seismic crustal structure and morphotectonic features associated with the Chain fracture zone and their role in the evolution of the equatorial Atlantic region. *Journal of Geophysical Research: Solid Earth*, *125*(10), e2020JB020275. https://doi.org/10.1029/2020jb020275

McKenzie, D., Jackson, J., & Priestley, K. (2005). Thermal structure of oceanic and continental lithosphere. *Earth and Planetary Science Letters*, *233*(3–4), 337–349. https://doi.org/10.1016/j.epsl.2005.02.005

Mehouachi, F., & Singh, S. C. (2018). Water-rich sublithospheric melt channel in the equatorial Atlantic Ocean. *Nature Geoscience*, *11*(1), 65–69. https://doi.org/10.1038/s41561-017-0034-z

Müller, R. D., Sdrolias, M., Gaina, C., & Roest, W. R. (2008). Age, spreading rates, and spreading asymmetry of the world's ocean crust. *Geochemistry, Geophysics, Geosystems*, *9*(4), Q04006. https://doi.org/10.1029/2007GC001743

Müller, R. D., Seton, M., Zahirovic, S., Williams, S. E., Matthews, K. J., Wright, N. M., et al. (2016). Ocean basin evolution and global-scale reorganization events since Pangea breakup. *Annual Review of Earth and Planetary Sciences*, *44*(1), 107–138. https://doi.org/10.1146/annurev-earth-060115-012211

Müller, R. D., Zahirovic, S., Williams, S. E., Cannon, J., Seton, M., Bower, D. J., et al. (2019). A global plate model including lithospheric deformation along major rifts and orogens since the Triassic. *Tectonics*, *38*(6), 1884–1907. https://doi.org/10.1029/2018TC005462

Pribnow, D., Kinoshita, M., & Stein, C. A. (2000). Thermal data collection and heat flow recalculations for ODP Legs 101-180. Retrieved from http://www-odp.tamu.edu/publications/heatflow/

Ren, Y., Geersen, J., & Grevemeyer, I. (2022). Impact of spreading rate and age-offset on oceanic transform fault morphology. *Geophysical Research Letters*, *49*(2), e2021GL096170. https://doi.org/10.1029/2021gl096170

Robinson, D. P. (2011). A rare great earthquake on an oceanic fossil fracture zone. *Geophysical Journal International*, *186*(3), 1121–1134. https://doi.org/10.1111/j.1365-246X.2011.05092.x

Roland, E., Behn, M. D., & Hirth, G. (2010). Thermal-mechanical behavior of oceanic transform faults: Implications for the spatial distribution of seismicity. *Geochemistry, Geophysics, Geosystems*, *11*(7), Q07001. https://doi.org/10.1029/2010GC003034

Roland, E., Lizarralde, D., McGuire, J. J., & Collins, J. A. (2012). Seismic velocity constraints on the material properties that control earthquake behavior at the Quebrada-Discovery-Gofar transform faults, East Pacific Rise. *Journal of Geophysical Research*, *117*(B11), B11102. https://doi.org/10.1029/2012JB009422

Ruddiman, W., Sarnthein, M., & Baldauf, J. (1988). *Proceedings of the ocean drilling program, Initial Reports* (Vol. 108, pp. 657–668). Ocean Drilling Program. https://doi.org/10.2973/odp.proc.ir.108.1988

Sandwell, D. T. (1984). Thermomechanical evolution of oceanic fracture zones. *Journal of Geophysical Research*, *89*(B13), 11401–11413. https://doi.org/10.1029/JB089iB13p11401

Sandwell, D. T., Müller, R. D., Smith, W. H. F., Garcia, E., & Francis, R. (2014). New global marine gravity model from CryoSat-2 and Jason-1 reveals buried tectonic structure. *Science*, *346*(6205), 65–67. https://doi.org/10.1126/science.1258213

Schilling, J. G., Ruppel, C., Davis, A. N., McCully, B., Tighe, S. A., Kingsley, R. H., & Lin, J. (1995). Thermal structure of the mantle beneath the equatorial Mid-Atlantic Ridge: Inferences from the spatial variation of dredged basalt glass compositions. *Journal of Geophysical Research*, *100*(B6), 10057–10076. https://doi.org/10.1029/95jb00668

Seton, M., Whittaker, J. M., Wessel, P., Müller, R. D., DeMets, C., Merkouriev, S., et al. (2014). Community infrastructure and repository for marine magnetic identifications. *Geochemistry, Geophysics, Geosystems*, *15*(4), 1629–1641. https://doi.org/10.1002/2013GC005176

Spinelli, G. A., Giambalvo, E. R., & Fisher, A. T. (2004). Sediment permeability, distribution, and influence on fluxes in oceanic basement. In E. E. Davis & H. Elderfield (Eds.), *Hydrogeology of the oceanic lithosphere (Issue April 2014)*. Cambridge University Press.

Stakes, D. S., Trehu, A. M., Goffredi, S. K., Naehr, T. H., & Duncan, R. A. (2002). Mass wasting, methane venting, and biological communities on the Mendocino transform fault. *Geology*, *30*(5), 407–410. https://doi.org/10.1130/0091-7613(2002)030<0407:MWMVAB>2.0.CO;2

Stein, C. A., & Stein, S. (1992). A model for the global variation in oceanic depth and heat flow with lithospheric age. *Nature*, *359*(6391), 123–129. https://doi.org/10.1038/359123a0

Stein, C. A., & Stein, S. (1994). Constraints on hydrothermal heat flux through the oceanic lithosphere from global heat flow. *Journal of Geophysical Research*, *99*(B2), 3081–3095. https://doi.org/10.1029/93JB02222

Swift, S. A., Kent, G. M., Detrick, R. S., Collins, J. A., & Stephen, R. A. (1998). Oceanic basement structure, sediment thickness, and heat flow near Hole 504B. *Journal of Geophysical Research*, *103*(B7), 15377–15391. https://doi.org/10.1029/98JB00698

Sykes, T. J. S. (1996). A correction for sediment load upon the ocean floor: Uniform versus varying sediment density estimations—Implications for isostatic correction. *Marine Geology*, *133*(1–2), 35–49. https://doi.org/10.1016/0025-3227(96)00016-3

USGS. (2020). Earthquake catalog. Retrieved from https://earthquake.usgs.gov

Vacquier, V., & von Herzen, R. P. (1964). Evidence for connection between heat flow and the mid-Atlantic ridge magnetic anomaly. *Journal of Geophysical Research*, *69*(6), 1093–1101. https://doi.org/10.1029/jz069i006p01093

Van Avendonk, H. J. A., Harding, A. J., Orcutt, J. A., & McClain, J. S. (1998). A two-dimensional tomographic study of the Clipperton transform fault. *Journal of Geophysical Research*, *103*(B8), 17885–17899. https://doi.org/10.1029/98JB00904

Villinger, H. W., Tréhu, A. M., & Grevemeyer, I. (2010). Seafloor marine heat flux measurements and estimation of heat flux from seismic observations of bottom simulating reflectors. In M. Riedel, E. C. Willough by, & S. Chopra (Eds.), *Geophysical characterization of gas hydrates* (pp. 279–300). Society of Exploration Geophysicists.

Villinger, H., & Davis, E. E. (1987). A new reduction algorithm for marine heat flow measurements. *Journal of Geophysical Research*, *92*(B12), 846–856. https://doi.org/10.1029/jb092ib12p12846

von Herzen, R., & Simmons, G. (1972). Two heat flow profiles across the Atlantic Ocean. *Earth and Planetary Science Letters*, *15*(1), 19–27. https://doi.org/10.1016/0012-821x(72)90024-6

Wang, K. (2004). Applying fundamental principles and mathematical models to understand processes and estimate parameters. In E. E. Davis & H. Elderfield (Eds.), *Hydrogeology of the oceanic lithosphere* (pp. 376–413). Cambridge University Press.

Wang, K., & Davis, E. E. (2003). High permeability of young oceanic crust constrained by thermal and pressure observations. In M. Taniguchi, K. Wang, & T. Gamo (Eds.), *Land and marine hydrogeology* (pp. 165–188). Elsevier.

Wang, Z., Singh, S. C., Prigent, C., Gregory, E., & Marjanovic, M. (2022). Deep hydration and lithospheric thinning at oceanic transform plate boundaries. *Nature Geoscience*, *15*(9), 741–746. https://doi.org/10.1038/s41561-022-01003-3

Wangen, M. (2010). *Physical principles of sedimentary basin analysis*. Cambridge University Press.

Wessel, P., Smith, W. H. F., Scharroo, R., Luis, J., & Wobbe, F. (2013). Generic mapping tools: Improved version released. *Eos, Transactions American Geophysical Union*, *94*(45), 409–410. https://doi.org/10.1002/2013eo450001